

**Three-dimensional coherent structures of electrokinetic instability**

E. A. Demekhin\*

*Department of Computation Mathematics and Computer Science, Kuban State University, Krasnodar, 350040, Russian Federation and Laboratory of General Aeromechanics, Institute of Mechanics, Moscow State University, Moscow, 117192, Russian Federation*

N. V. Nikitin

*Laboratory of General Aeromechanics, Institute of Mechanics, Moscow State University, Moscow, 117192, Russian Federation*

V. S. Shelistov

*Scientific Research Department, Kuban State University, Krasnodar, 350040, Russian Federation*

(Received 13 February 2014; published 31 July 2014)

A direct numerical simulation of the three-dimensional electrokinetic instability near a charge-selective surface (electric membrane, electrode, or system of micro- or nanochannels) has been carried out and analyzed. A special finite-difference method has been used for the space discretization along with a semi-implicit  $3\frac{1}{3}$ -step Runge-Kutta scheme for the integration in time. The calculations employ parallel computing. Three characteristic patterns, which correspond to the overlimiting currents, are observed: (a) two-dimensional electroconvective rolls, (b) three-dimensional regular hexagonal structures, and (c) three-dimensional structures of spatiotemporal chaos, which are a combination of unsteady hexagons, quadrangles, and triangles. The transition from (b) to (c) is accompanied by the generation of interacting two-dimensional solitary pulses.

DOI: [10.1103/PhysRevE.90.013031](https://doi.org/10.1103/PhysRevE.90.013031)

PACS number(s): 47.57.jd, 47.61.Fg, 47.20.Ky

**I. INTRODUCTION**

Problems of electrokinetics and micro- and nanofluidics have recently attracted a great deal of attention due to rapid developments in micro-, nano-, and biotechnology. Among the numerous modern micro- and nanofluidic applications of electrokinetics are micropumps, micromixers,  $\mu$ TAs, desalination, fuel cells, etc. (see [1]).

Usually in such systems, the applied electric currents do not exceed the limiting current. Recent practice in electrodialysis and related problems has demonstrated the interest in using intensive current regimes, wherein the applied current exceeds its limiting value. Another interesting discovery has been the nonstationary overlimiting currents, resulting in increased ion transfer to the charge-selective surface because of a specific type of electrohydrodynamic instability: the electrokinetic instability. Motivated by the applications mentioned, we revisit the classical problem of electrodialysis, taking into account the electrokinetic instability in a full three-dimensional formulation. Another motivation is connected with the fundamental interest in this type of instability at the micro- and nanoscales. In the present study, traditional macroscopic approximations of a continuous medium are applied over the whole spatial region, which includes the Debye layer, the extended space charge (ESC), and vortex regions.

Micro- and nanofluidic systems pose interesting problems for applied mathematics because the traditional macroscopic approximations of a continuous medium break down at small scales approaching the Debye length. To provide some perspective on our problem, the Debye layer, depending on the ion concentration, varies within the range of 1 to 100 nm. The ESC length is about 200 to 500 nm, and depends on the

voltage, and the electroconvective vortex length is about the distance between the membranes, i.e., about 0.1 to 1.5 mm. Taking into account a rough evaluation of the length scale at which the continuous approximation breaks down, 10 nm for liquids [2], we can say that in the region of the Debye layer, the continuous model is questionable, while in the ESC and vortex regions it seems to be applicable. The nanoscale Debye and ESC regions are not detectable in experiments, but the microvortices and macroscale coherent structures sustained by them have been found experimentally (see [1], Fig. 6; [3], Fig. 3(a); [4], Fig. 3). Chaotic behavior can be seen in chronopotentiograms, time vs voltage, Ref. [5], Fig. 1, but it is very difficult to relate this with the real behavior in the Debye region. Hence the comparison of our numerics with DNS results based on other models is promising, in particular, with the lattice Boltzmann method (LBM) [6], which is straightforwardly adaptable for parallel computing. Moreover, a hybrid framework, combining mesoscopic LBM in the Debye layer with a macroscopic continuous method in the ESC and vortex regions, is worthwhile. Nevertheless, in what follows, we employ only the traditional macroscopic approximations of a continuous medium.

The electrokinetic instability describes the generation of nonlinear coherent structures near a charge-selective surface under a drop in the electric potential. This instability was recently theoretically predicted by Rubinstein and Zaltzman [7–9] and experimentally confirmed in [3,4,10–13]. The linear stability theory of the one-dimensional (1D) quiescent steady-state solution, based on a systematic asymptotic analysis of the problem, was developed by Zaltzman and Rubinstein [14]. Different aspects of the linear stability of the 1D solution were also studied in [15–17]. A qualitative discussion of the basic mechanisms of the electrokinetic instability can be found in [18]. The two-dimensional electroconvective rolls generated by surfaces bearing a charge varying in space are considered in

\*edemekhi@gmail.com

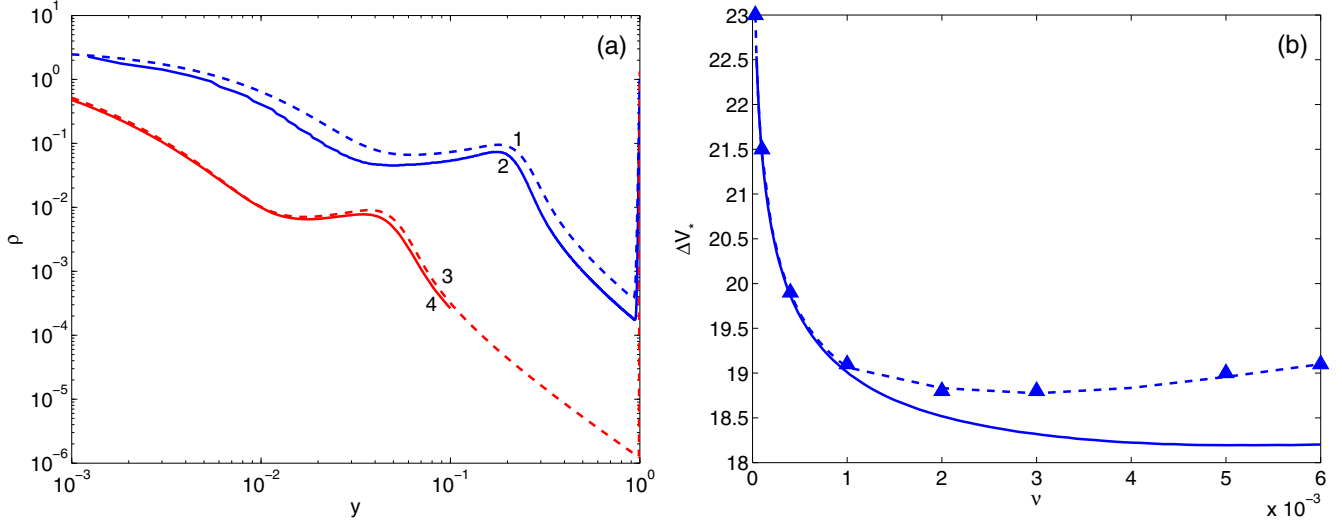


FIG. 1. (Color online) Comparison of our numerical predictions, dashed line, with those by Zaltzman and Rubinstein [14], solid line,  $\kappa = 0.5$ . (a) Space-charge density,  $\rho$ , vs  $y$  for  $\Delta V = 20$  and  $\nu/\sqrt{2} = 10^{-2}$  (lines 1 and 2) and  $10^{-3}$  (lines 3 and 4). (b) Threshold of the primary instability: triangles stand for our numerics.

[19]. The electrokinetic instability is reminiscent of Rayleigh-Bénard convection [20], but from both the physical and mathematical points of view, it is much more complicated. The Reynolds number in the electrokinetic instability is very small and, hence, the dissipation is very large and the nonlinear terms in the Navier-Stokes system are negligibly small. The nonlinearity responsible for bifurcations arises from other equations of the system. This explains the dramatic distinction between the bifurcations, instabilities, and transitions in the macro- and microhydrodynamics.

Not all important facts of the electrokinetic instability can be described by an asymptotic analysis and linear stability theory. Only direct numerical simulations (DNS) of the Nernst-Planck-Poisson-Navier-Stokes equations can be relied on in the study of all the details of the electrokinetic instability. In the first DNS studies [5,21–26], the nontrivial stages of a noise-driven nonlinear evolution towards overlimiting regimes were identified, the space charge in the extended space-charge region was found to have a typical spikelike distribution, the dynamics of the spikes was investigated along with the physical mechanisms of the secondary instabilities, and it was demonstrated that the transition between the limiting and the overlimiting current regimes can exhibit a hysteretic behavior (subcritical bifurcation).

All the previous results were obtained in the two-dimensional (2D) formulation. Actually, the electrokinetic instability is three dimensional (3D) and such a fact should dramatically affect the DNS results. In the present paper, 3D numerical simulations of the electrokinetic instability are carried out. White-noise initial conditions to mimic “room disturbances” and the subsequent natural evolution of the solution are treated. The following regimes, which replace each other as the potential drop between the selective surfaces increases, are obtained: a 1D quiescent steady-state solution, 2D steady electroconvective rolls (vortices), unsteady 2D vortices regularly or chaotically changing their parameters, steady 3D hexagonal patterns, and a chaotic spatiotemporal 3D motion.

The space-charge region profile for the 2D rolls has long flat and short wedgelike regions with a cusp at the top. The cusp angle does not depend on the parameters and is about  $111^\circ$ . The 3D hexagonal structures consist of six wedgelike lateral faces, and six pyramids are located at their intersection. The angle of the wedgelike faces is close to that for the 2D rolls, and the dependence of this angle on the parameters of the problem is also weak. A rough evaluation of the pyramidal angle gives its value as about  $87^\circ$ .

An interesting phenomenon found is the generation of two-dimensional running solitary waves either inside the hexagonal structure or at one of its lateral sides. If another solitary wave forms, a complex head-on or an oblique pulse-pulse interaction occurs. For a large potential drop, the pulse-pulse interaction becomes strong enough to destroy the hexagonal structure and a transition to spatiotemporal chaos results.

## II. FORMULATION OF THE PROBLEM

A symmetric, dilute binary electrolyte with a diffusivity of cations and anions  $\tilde{D}$ , dynamic viscosity  $\tilde{\mu}$ , and electric permittivity  $\tilde{\epsilon}$ , and bounded by ideal, semiselective ion-exchange membrane surfaces,  $\tilde{y} = 0$  and  $\tilde{y} = \tilde{L}$ , is considered. Tildes indicate the dimensional variables, as opposed to their dimensionless counterparts without tildes.  $\tilde{x}$ ,  $\tilde{y}$ , and  $\tilde{z}$  are the coordinates, where  $\tilde{x}$  and  $\tilde{z}$  are directed along the membrane surface, and  $\tilde{y}$  is normal to it.

The characteristic quantities to make the system dimensionless are as follows:  $\tilde{L}$  is the distance between the membranes;  $\tilde{L}^2/\tilde{D}$  is the characteristic time; the dynamic viscosity  $\tilde{\mu}$  is taken as the characteristic dynamical quantity; the thermic potential  $\tilde{\Phi}_0 = \tilde{R}\tilde{T}/\tilde{F}$  is taken as the characteristic potential; and the bulk ion concentration at the initial time  $\tilde{c}_0$  is the characteristic concentration. Here,  $\tilde{F}$  is Faraday’s constant,  $\tilde{R}$  is the universal gas constant, and  $\tilde{T}$  is the absolute temperature.

The electroconvection is described by the equations for ion transport, Poisson's equation for the electric potential, and the Stokes equations for a creeping flow:

$$\frac{\partial c^\pm}{\partial t} + \mathbf{u} \cdot \nabla c^\pm = \pm \nabla \cdot (c^\pm \nabla \Phi) + \nabla^2 c^\pm, \quad (1)$$

$$\nu^2 \nabla^2 \Phi = c^- - c^+ \equiv -\rho,$$

$$-\nabla \Pi + \nabla^2 \mathbf{u} = \frac{\kappa}{\nu^2} \rho \nabla \Phi, \quad \nabla \cdot \mathbf{u} = 0. \quad (2)$$

Here, the  $c^\pm$  are the concentrations of the cations and anions;  $\mathbf{u} = \{u, v, w\}$  is the fluid velocity vector;  $\Phi$  is the electrical potential;  $\Pi$  is the pressure;  $\nu$  is the dimensionless Debye length or Debye number,

$$\nu = \frac{\tilde{\lambda}_D}{\bar{L}}, \quad \tilde{\lambda}_D = \left( \frac{\tilde{\varepsilon} \tilde{\Phi}_0}{\tilde{F}^2 \tilde{c}_0} \right)^{1/2} = \left( \frac{\tilde{\varepsilon} \tilde{R} \tilde{T}}{\tilde{F}^2 \tilde{c}_0} \right)^{1/2},$$

and  $\kappa = \tilde{\varepsilon} \tilde{\Phi}_0^2 / \mu \tilde{D}$  is a coupling coefficient between the hydrodynamics and the electrostatics that characterizes the physical properties of the electrolyte solution and is fixed for a given pair of liquid and electrolyte.

This system of dimensional equations is complemented by the proper conditions at the lower and upper boundaries,  $y = 0$  and  $y = 1$ :

$$c^+ = p, \quad -c^- \frac{\partial \Phi}{\partial y} + \frac{\partial c^-}{\partial y} = 0, \quad \mathbf{u} = 0. \quad (3)$$

The potential drop between the membranes is  $\Delta V$ .

The first boundary condition, prescribing an interface concentration equal to that of the fixed charges inside the membrane, is asymptotically valid for large  $p$  and was first introduced by Rubinstein; see, for example, Ref. [14]. The second boundary condition means there is no flux for negative ions, and the last condition is that the velocity vanishes at the rigid surface. The spatial domain is assumed to be infinitely large in the  $x$  and  $z$  directions, and the boundedness of the solution as  $x, z \rightarrow \pm\infty$  is imposed as a condition.

Adding initial conditions for the cations and anions completes the formulation (1)–(3). These initial conditions arise from the following viewpoint: when there is no potential difference between the membranes, the distribution of ions is homogeneous and neutral. This corresponds to the condition  $c^+ = c^- = 1$ . Some kind of perturbation should be superimposed on this distribution, which is natural from the viewpoint of experiment.

Small-amplitude disturbances at the initial stage of evolution can be considered as a superposition of individual harmonics that obeys the linear stability theory and will soon filter the initial noise into a sharp frequency band near the maximum growth rate (see [21], Fig. 3, and [27], Figs. 3 and 5). That is why the nature of the noise is not important if the initial spectrum contains nonzero harmonics near the frequency with the maximum growth rate. The simplest type of initial noise is taken: the so-called “room disturbances” determining the external low-amplitude and broadband white noise are imposed on the concentration:

$$t = 0: c^\pm = 1 + \int_{-\infty}^{+\infty} \hat{c}^\pm(k, m) e^{-i(kx+mz)} dk dm. \quad (4)$$

Here, the phase of the complex function  $\hat{c}^\pm(k, m)$  is assumed to be a random number with a uniform distribution over the interval  $[0, 2\pi]$ .

The characteristic electric current  $j$  at the membrane's surface is referred to the limiting current,  $j_{\text{lim}} = 4$ ,

$$j = \frac{1}{4} \left( c^+ \frac{\partial \Phi}{\partial y} + \frac{\partial c^+}{\partial y} \right) \quad \text{for } y = 0. \quad (5)$$

It is also convenient for our further analysis to introduce the electric current averaged over the membrane's surface  $l_x \times l_z$  and over time:

$$\langle j(t) \rangle = \frac{1}{l_x l_z} \int_0^{l_x} \int_0^{l_z} j(x, z, t) dx dz, \quad (6)$$

$$J = \lim_{T \rightarrow \infty} \frac{1}{T} \int_0^T \langle j(t) \rangle dt.$$

The problem is characterized by three dimensionless parameters:  $\Delta V$ ,  $\nu$  (which is a small parameter), and  $\kappa$ . The dependence on the concentration,  $p$ , for the overlifting regimes is practically absent, and thus  $p$  is not included in the mentioned parameters: in all calculations,  $p = 5$ .

The problem is solved for  $\kappa = 0.05$ – $0.5$ , and the dimensionless potential drop is varied within  $\Delta V = 0$ – $60$ . In most of the presented calculations,  $\nu = 10^{-3}$  is taken.

### III. NUMERICAL METHOD

The numerical approach of [5] is generalized for the solution of the system (1)–(6). A finite-difference method with second-order accuracy is applied for the spatial discretization. A uniform grid is used in the homogeneous tangential  $x$  and  $z$  directions; the grid is stretched in the normal  $y$  direction via a tanh stretching function in order to properly resolve the thin double layers attached to the membrane surfaces. When a fine spatial resolution is used, our system represents a stiff problem. In order to solve this problem, implicit methods require the inversion of rather large matrices and thus are extremely costly, while explicit methods of time advancement require a very small time step and, hence, are prohibitively ineffective. A semi-implicit method is found to be a reasonable compromise: only a part of the right-hand side of the system is treated implicitly [28]. A special semi-implicit  $3\frac{1}{3}$ -step Runge-Kutta scheme is used for the eventual integration in time. The details of the numerical scheme will be presented elsewhere.

For the natural “room disturbances,” the infinite spatial domain is changed to a large enough finite domain that has lengths  $l_x = l_z = l$  in both spatial dimensions, with the corresponding wave number  $k = 2\pi/l$ . The condition that the solution be bounded as  $x, z \rightarrow \infty$  is changed to periodic boundary conditions. The length of the domain  $l$  has to be taken large enough to make the solution independent of the domain size. The wave number  $k$  is taken to be 1.

The parallel computing was carried out at the supercomputer “Chebyshev” of the computer cluster SKIF of the Moscow State University, using up to 256 MPI processors. A resolution of 256 points in the  $x$  and  $z$  directions along with 128 points in the  $y$  direction provides adequate results. In order

to check their accuracy, the number of points in all directions for some simulations was doubled.

#### IV. SIMULATION RESULTS

The system (1)–(6) has a 1D quiescent steady-state solution which describes the underlimiting and limiting currents. For the limiting currents, there is a thin electric double layer (EDL) in a small vicinity of the charge-selective surface; then an equilibrium diffusion layer forms right next to this surface, and the voltage-current (VC) curve obeys a linear ohmic relation. For the limiting currents, the VC curve has a typical saturation of the electric current with respect to the potential drop. In order to explain this behavior, Rubinstein and Shtilman [29] came up with the idea of the nonequilibrium nature of the EDL and of the extended space charge (ESC) region,  $0 < y < y_m$ , which is much thicker than the EDL, but much thinner than the distance between the membranes,  $y_m \ll 1$ . For the underlimiting and limiting currents, the diffusion is balanced by electromigration: there is no contribution of convection to the ion flux, and the ESC layer thickness,  $y_m$ , is uniform along the membrane surface. (The boundary of the ESC region,  $y_m$ , gives a convenient value for describing the electrokinetic patterns. This boundary is a conventional value: we define it by taking 5% of the maximal value of the space-charge density in the ESC region.)

The appearance of the extended space charge for the limiting current regimes leads to a special kind of electrohydrodynamic instability, when  $\Delta V > \Delta V_*$ : the electrokinetic instability (see [7,8,14]). A small inhomogeneity in  $y_m(x, z)$  along the membrane results in a convective motion of the fluid in the inner ESC region with a tangential slip velocity, and leads to the growth of the perturbations: the 1D steady-state equilibria lose their stability and, eventually, overlimiting currents arise. For the overlimiting currents, the third mechanism, convection, contributes significantly to the ion flux.

The key physical mechanism of the primary instability can be understood from the following simple arguments. The ESC region creates a thin film near the membrane,  $y_m \ll 1$ , much like a free surface. When the ESC layer,  $y_m$ , thins because of some kind of localized disturbance along the membrane, the nearly singular electric field  $\mathbf{E}$  inside the ESC region becomes even more intense, thus creating a high Maxwell pressure spot near the charge-selective surface,  $\sim E^2$ . This high-pressure spot drives liquid radially away from it near the solid surface. When the displaced liquid moves, it meets some resistance from the nonslipping liquid layers, and this changes the direction of the moving liquid towards the bulk. As a result, a pair of vortices rotating in opposite directions appears, both with a diverging stagnation point. These electroconvective vortices which arise near the critical point  $\Delta V_*$  are two dimensional.

Before the systematic calculations, we validate our numerical results first to assure that the predictions are correct. The comparison of our predictions with those predicted by Zaltzman and Rubinstein [14] using the asymptotical analysis for small voltages is shown in Fig. 1. For a small enough Debye number  $\nu$ ,  $\nu < 10^{-3}$ , the results of both approaches coincide with graphical accuracy.

In Fig. 2, a map of the regimes and bifurcations is presented: the first coordinate is the potential drop  $\Delta V$  and the other is the

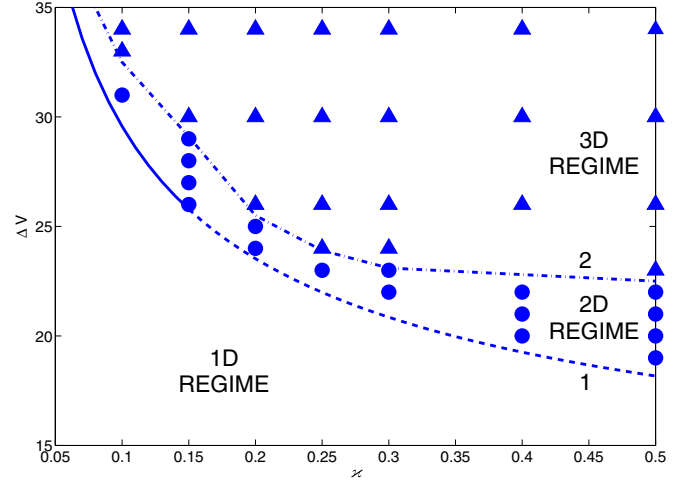


FIG. 2. (Color online) Map of regimes and bifurcations,  $\Delta V$ , vs  $\kappa$  for  $\nu = 10^{-3}$ . The solid line is the neutral stability curve [5] which separates the 1D and 2D regimes. Circles correspond to realizations of 2D regimes; triangles correspond to realizations of 3D regimes, so that the 2D–3D transition happens at the dash-dot line.

coupling coefficient  $\kappa$ . Curve 1 corresponds to the threshold of instability: for  $\kappa < 0.151$ , the bifurcation is supercritical and this part of 1 is pictured by the solid line; for  $\kappa > 0.151$ , the bifurcation is subcritical and this part of the curve is shown by the dashed line (see [5]). The 1D regimes and the limiting currents are located below 1. The circles and triangles stand for the 2D and 3D regimes, respectively. The dash-dot line 2 separates these regimes and corresponds to the 2D–3D transition.

The dependence on the potential drop  $\Delta V$  of the average of the electric current  $J$  over the membrane surface  $l_x l_z = l^2$  and the elapsed time  $t$  [see Eq. (5)] is a convenient integral characteristic of the regimes. Such a VC dependence is shown in Fig. 3 for a typical value of the coupling coefficient  $\kappa = 0.1$ , where the bifurcation is supercritical. Portions of the VC dependence, I, II, and III, stand for the underlimiting, limiting, and overlimiting currents, respectively. The dashed line in Fig. 3 joining the circles corresponds to 3D simulations. We find it instructive to plot in this figure also the results of the 2D simulations: they are shown by the dashed line joining the triangles corresponding to the 2D simulations. Up to the point  $\Delta V = \Delta V_{3D}$ , both dependences coincide. This means that for a small supercriticality, the electrokinetic instability is two dimensional. This points to the fact that 3D effects increase the ion flux in comparison with the two-dimensional regime, but this increase is not large, about 5%–10%. Moreover, for a large enough potential drop,  $\Delta V > 55$ , this difference practically disappears.

Our simulations show that four basic coherent structures can be found during the evolution: 2D electroconvective rolls (vortices), squares, triangles, and hexagons.

(a) The first coherent structure, spatially periodic stationary electroconvective rolls, can be realized as an attractor, as  $t \rightarrow \infty$ , only in a narrow band near the threshold of instability, between curves 1 and 2 of Fig. 2. This is reminiscent of the Rayleigh–Bénard convection (see [30,31]) when hexagons and squares are unstable to rolls, near the threshold, and there is

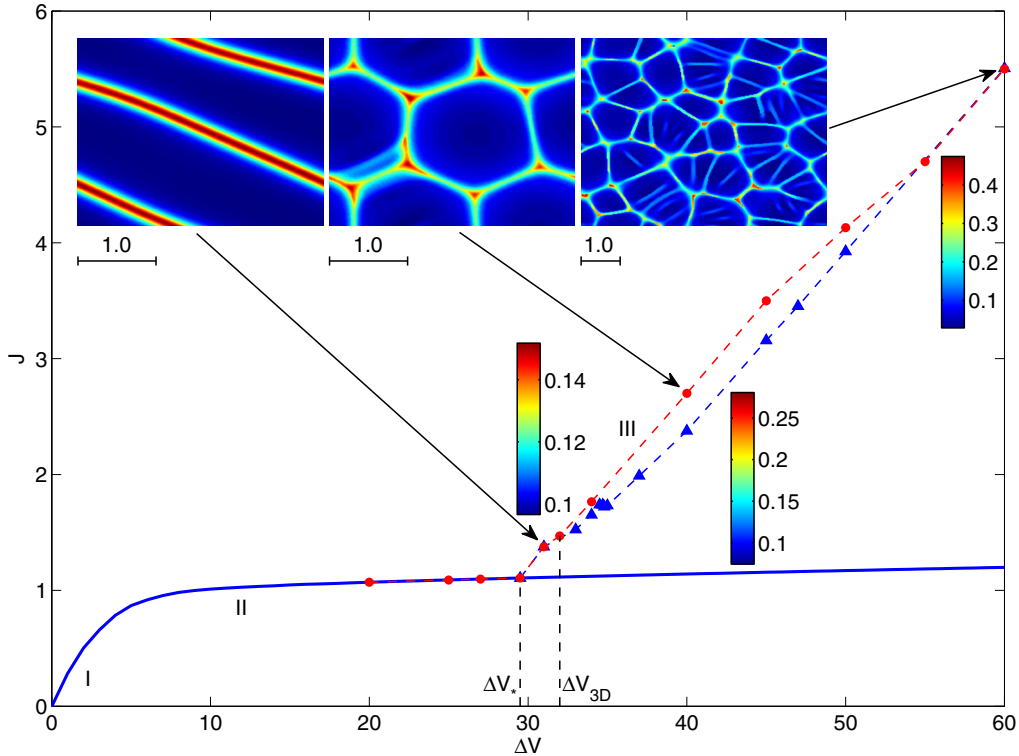


FIG. 3. (Color online) VC characteristics for  $\kappa = 0.1$  and  $\nu = 10^{-3}$ : I, II, and III stand for underlimiting, limiting, and overlimiting currents, respectively. The dashed line joining the circles corresponds to our 3D simulations; the dashed line joining the triangles corresponds to 2D simulations. The inset shows three typical electrokinetic patterns: 2D electroconvective rolls, regular 3D hexagonal structures, and chaotic 3D structures.

a closed region of their stability called the “Busse balloon.” Note that the bifurcation picture is different for the Bénard-Marangoni convection, where stable hexagonal patterns can arise at the threshold (see [32]). The two-dimensional coherent structures are of particular interest because of the relative simplicity of their investigation in the 2D formulation. These solutions were analyzed in detail in [5,21–25].

(b) For  $\Delta V > \Delta V_{3D}$ , above line 2 of Fig. 2, the 2D electroconvective rolls become unstable to three-dimensional perturbations. Theoretically, there are three candidates to inherit stability and be a new attractor: squares, triangles, and hexagons [30]. Our simulations show that for the electrokinetic instability, steady and regular squares and triangles do not exist: they can be seen during the evolution only as a transitional state.

(c) Regular steady-state hexagonal patterns are formed just above line 2 of Fig. 2. The white-noise initial perturbations eventually evolve towards steady hexagonal patterns.

(d) As the driving  $\Delta V - \Delta V_*$  is increased, the ordered hexagonal structures break down into complex and highly disordered states, and the behavior becomes chaotic in time and space. The flow becomes a combination of unsteady hexagons, quadrangles, and triangles. In the present investigation, the advent of spatiotemporal chaos is found by visual inspection; in a future extension of this work, we intend to detect it by a calculation of the maximal Lyapunov exponent, as was done in [20].

To complete the VC dependence, three characteristic electrokinetic patterns are shown in the inset to Fig. 3: 2D

electroconvective vortices, regular 3D hexagonal structures, and chaotic 3D structures (combinations of unsteady hexagons, quadrangles, and triangles). The arrows show the place of these structures along the VC curve and a typical potential drop for their realization. A movie of the evolution of these structures can be found in [33].

Let us consider some important details of these characteristic patterns: the electroconvective rolls, the hexagons, and the spatiotemporal chaos. In order to present a full picture of the behavior, it is instructive to jointly analyze the distribution of  $y_m(x, z)$  along the membrane surface, the charge density  $\rho$  inside the ESC region, and the electric current  $j(x, z)$  determined by Eq. (5). Their typical snapshots are depicted in Figs. 4, 6, and 7.

For the rolls, the profile  $y_m(x, z)$  is shown in Fig. 4: it has long flat and short wedgelike regions with a cusp at the top. The wedge angle or the angle between the wedge faces is rather conservative, it practically does not depend on the parameters, and is about  $105^\circ$ – $118^\circ$ .

After loss of stability and after the corresponding secondary bifurcation, the rolls turn into steady three-dimensional structures. Since secondary instabilities occur in already complicated states, the range of possible classes is larger than at the primary instability threshold. Here we discuss only one possible physical mechanism of the secondary instability that leads to the loss of two dimensionality. The evolution of 2D rolls slightly disturbed along the third spatial dimension is presented in Fig. 5. The flat regions of  $y_m(x, z)$ , I and II, have different charge densities, namely, in the vicinity

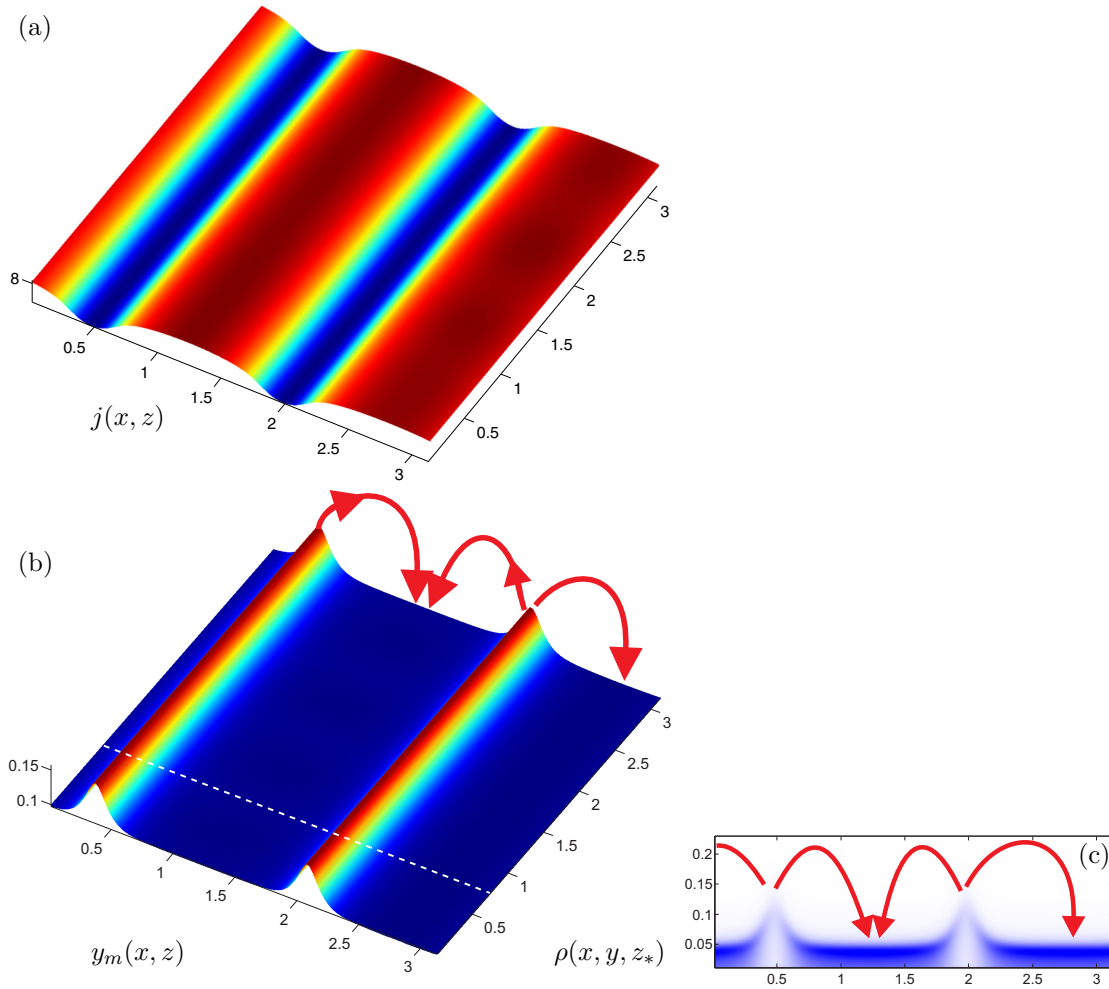


FIG. 4. (Color online) Electroconvective rolls for  $\Delta V = 33$ ,  $\kappa = 0.1$ , and  $\nu = 10^{-3}$ . (a) Distribution of the electric current  $j(x, z)$ . (b) Profile of  $y_m(x, z)$ . (c) Cross section of charge density  $\rho$  at  $z = z_*$ . Vortex pairs of liquid flow are shown schematically by the arrows.

of point 1, the charge density of the narrow part of II is smaller [see Fig. 5(a)] and, hence, the Coulomb force at II is also smaller (charges of the same sign repel). As a result, region I is nonuniformly expanding, while region II is nonuniformly narrowing, Fig. 5(b), with eventual coarsening at the narrowest part of II, Fig. 5(c). Another physical mechanism

of instability can be found: if the area of a flat region is large enough, it suffers from the primary electrokinetic instability; see Fig. 5(c). Point 1 is a nucleation point of a future electroconvective vortex.

The final result of the secondary instability is shown in Fig. 6: these steady structures are conventionally called

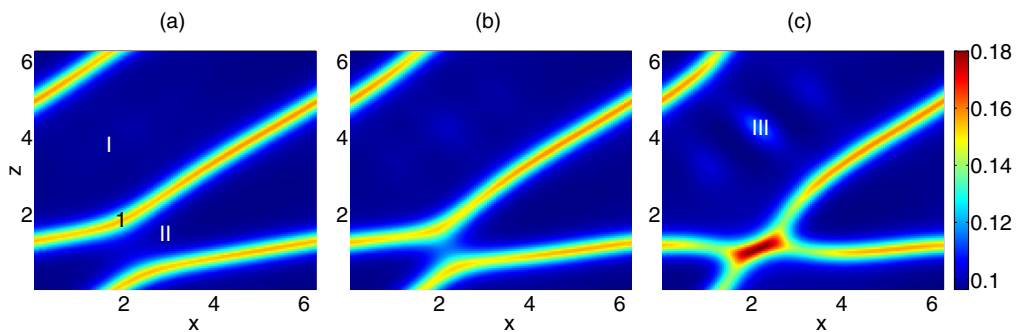


FIG. 5. (Color online) 2D–3D transition,  $\Delta V = 34$ , and  $\kappa = 0.1$ . Profiles of the ESR length,  $y_m(x, z)$ , at (a)  $t = 7.4$ . Flat region I near point 1 has a larger charge density than II; hence the Coulomb force of I at this point is larger than at II. This causes a further narrowing of II: (b)  $t = 7.5$ , with eventual coarsening, (c)  $t = 7.6$ . Region III is a nucleating region of a future electroconvective vortex caused by the primary instability.

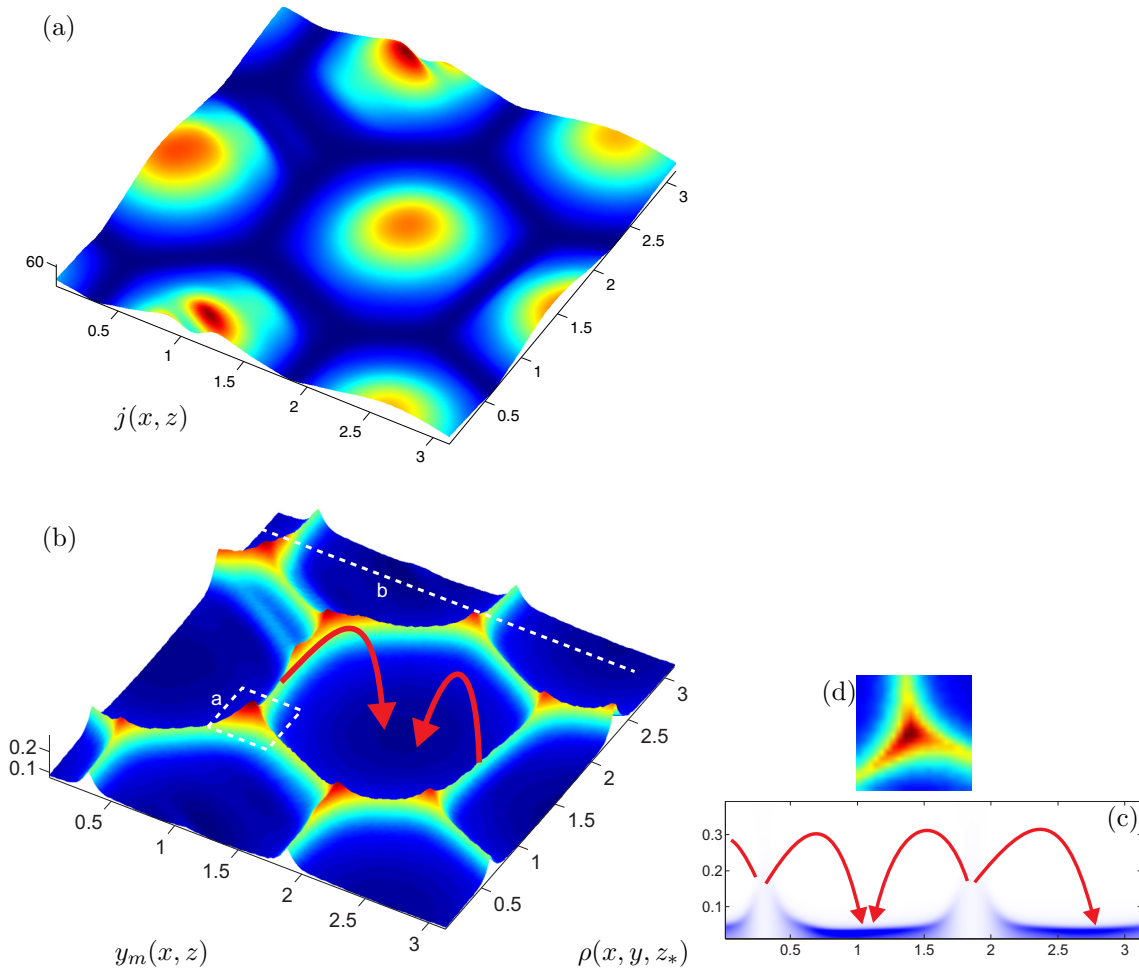


FIG. 6. (Color online) Hexagonal coherent structures,  $\Delta V = 50$ ,  $\kappa = 0.1$ , and  $\nu = 10^{-3}$ . (a) Distribution of the electric current  $j(x,z)$  on the membrane surface. (b) Profile of ESC region,  $y_m(x,z)$ : (c) cross section  $z = z_*$  of the charge density  $\rho$ ; (d) vicinity of the pyramid top. The arrows schematically show the direction of the liquid flow.

“hexagons.” The  $y_m(x,z)$  profile consists of six wedgelike lateral faces and six pyramids are located at their intersection. In the remaining area,  $y_m(x,z)$  is flat and situated in the lowlands. It is interesting that the angle of wedgelike faces is close to that for the 2D rolls, and the dependence of this angle on the parameters of the problem is also weak. A rough evaluation of the pyramidal angle gives its value as about  $85^\circ$ – $90^\circ$ .

Snapshots of the spatiotemporal chaos are shown in Fig. 7. Now, the  $y_m(x,z)$  distribution consists of a combination of triangles, quadrangles, and hexagons whose location and form change chaotically. The sides of these geometrical figures are wedges with an angle averaged over time of about  $110^\circ$ . The pyramids formed at the intersection of the sides have a time-averaged angle at the top of about  $90^\circ$ .

The numerical resolution of the charge density  $\rho$  in the thin ESC layer is shown for our three basic patterns in the left part of Figs. 4, 6, and 7. The darker regions correspond to large charge densities  $\rho$  with a rather sharp boundary between the ESC region,  $0 < y < y_m$ , and the diffusion region,  $y > y_m$ . The portions with a small charge in the spikes are joined by the flat regions of large charge. For all three regimes, the

minimum of  $y_m$  corresponds to the maximum of the charge density. At the top of the pyramids, where  $y_m(x,y)$  reaches its maximum maximum, the  $\rho$  distribution always has its minimum minimum.

The electric current at the membrane surface,  $j(x,z)$ , is another important characteristic value whose description complements our understanding of the system’s behavior; see the top of Figs. 4, 6, and 7. For all three basic coherent structures,  $j(x,z)$  qualitatively replicates the  $y_m(x,z)$  profile and  $\rho$  distribution in the ESC layer, but smooths their sharp details: for 2D rolls, the localized wedgelike profile of  $y_m(x,z)$  turns into the nearly sinusoidal profile of  $j(x,z)$ ; for the 3D regular patterns, the hexagon turns into a circle; the triangles, quadrangles, and hexagons of the spatiotemporal chaos transform into a system of circles and ellipses. Moreover, the electric current  $j(x,z)$  has minimal values in the vicinity of the cusps and is maximal in the flat regions of the  $y_m$  and  $\rho$  distributions. We attribute this behavior to the fact that the electrical conductivity is smaller in the cusp regions and larger in the lowlands.

Our simulations show that the liquid always flows upwards from the cusp points of the  $y_m$  and  $\rho$  distributions and

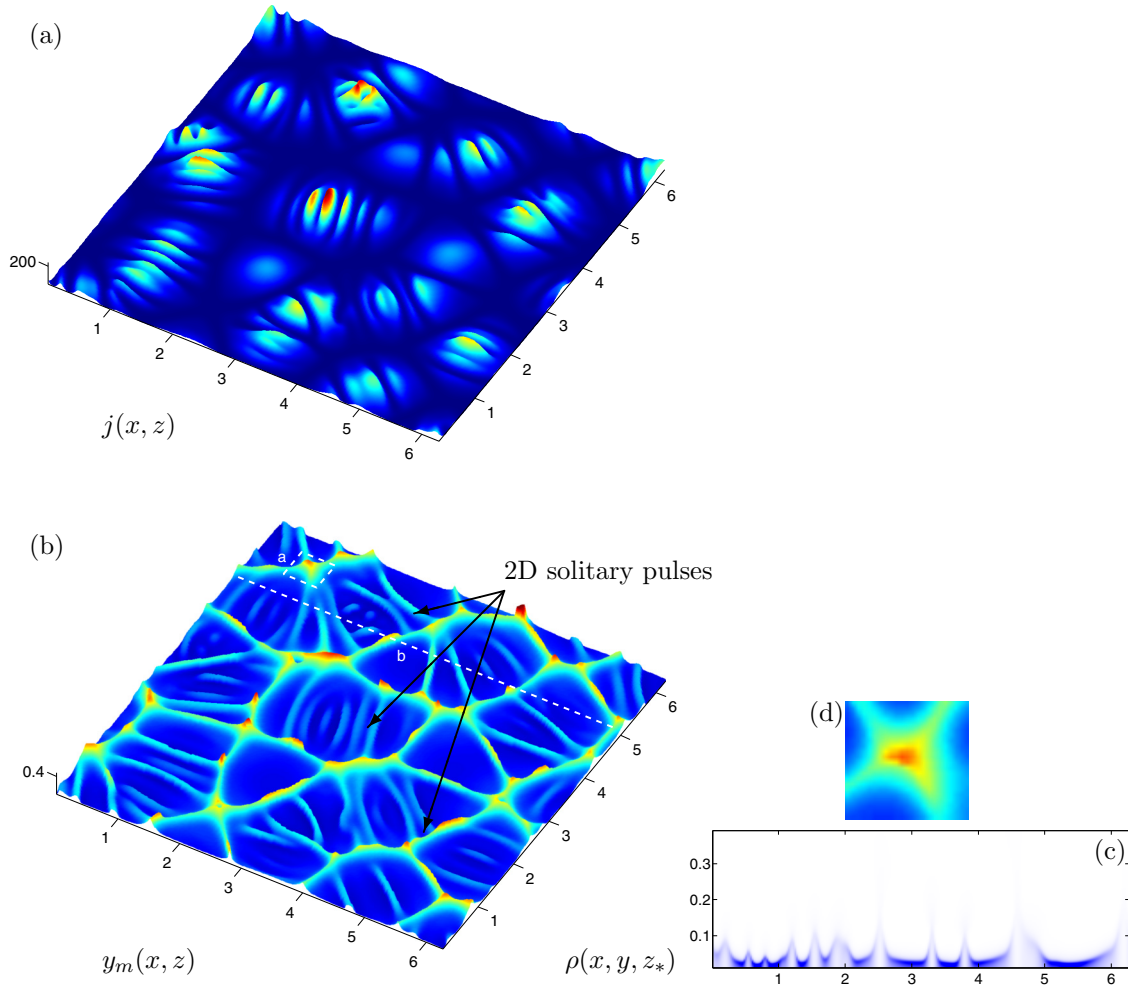


FIG. 7. (Color online) (a) Distribution of the electric current  $j(x,z)$  on the membrane surface. (b) Snapshot of  $y_m$  for the spatiotemporal chaos: (c) cross section  $z = z_*$  of the charge density  $\rho$ ; (d) vicinity of the pyramid top.  $\Delta V = 60$ ,  $\kappa = 0.1$ , and  $\nu = 10^{-3}$ .

returns to the membrane surface, moving towards the flat regions of the  $\rho$  distribution. An array of vortex pairs is formed: it is schematically shown in the figures by the arrows. The characteristic size of the electroconvective rolls varies within the range 1.3–2.0, the size of the regular hexagonal structures is about 1.5, and, for the spatiotemporal chaos, about 1.2.

An interesting phenomenon found is the generation of two-dimensional running solitary waves (pulses). Such waves form spontaneously either inside the hexagonal structure or at one of its lateral sides, with a subsequent propagation towards the opposite side of the hexagon; see Fig. 7. For relatively small drives  $\Delta V - \Delta V_*$ , the generation of a pulse is a rare event; moreover, the pulse decays during its propagation and eventually disappears completely. As  $\Delta V - \Delta V_*$  increases, this generation occurs more frequently, the pulse amplitude increases, and the pulse can propagate without decaying and reach the opposite side of the hexagon. If at the neighboring side or somewhere else another solitary wave forms and then departs, a complex pulse-pulse interaction occurs: depending on the spatial location of the waves, it can be a head-on or an oblique interaction. For large  $\Delta V - \Delta V_*$ , the pulse-pulse interaction becomes strong enough to destroy the hexagonal

structure and a transition to spatiotemporal chaos results from the interaction. Our systematic calculations were done for  $\nu = 10^{-3}$ , but in the region of spatiotemporal chaos we also performed several runs for  $\nu = 10^{-4}$  and  $\nu = 5 \times 10^{-4}$ ; the generation of solitary pulses and the pulse dynamics are found to be qualitatively the same as for  $\nu = 10^{-3}$ . Note that a similar phenomena of pulse generation and pulse-pulse interactions have been observed for other kinds of instability, Marangoni-Bénard convection [34,35], and falling liquid films [36].

### V. CONCLUSIONS

A direct numerical simulation of the electrokinetic instability in its three-dimensional formulation was carried out. A special numerical algorithm was developed. The calculations employed parallel computing. Three characteristic patterns, which correspond to the overlimiting currents, were observed: two-dimensional electroconvective rolls, three-dimensional regular hexagonal structures, and three-dimensional structures of spatiotemporal chaos that are combinations of unsteady hexagons, quadrangles, and triangles. The distinguishing features of the regular and chaotic three-dimensional regimes

were found. The transition from the steady regular three-dimensional patterns to the spatiotemporal chaos was found to be accompanied by the generation of interacting two-dimensional solitary pulses.

#### ACKNOWLEDGMENTS

This work was supported, in part, by the Russian Foundation for Basic Research (Projects No. 12-08-00924-a and No. 13-08-96536-r\_yug\_a).

- 
- [1] H.-C. Chang, G. Yossifon, and E. A. Demekhin, *Annu. Rev. Fluid Mech.* **44**, 401 (2012).
- [2] N.-T. Nguyen and S. T. Wereley, *Fundamentals and Applications of Microfluidics* (Artech House, London, 2006).
- [3] S. M. Rubinstein, G. Manukyan, A. Staicu, I. Rubinstein, B. Zaltzman, R. G. H. Lammertink, F. Mugele, and M. Wessling, *Phys. Rev. Lett.* **101**, 236101 (2008).
- [4] S. J. Kim, Y.-C. Wang, J. H. Lee, H. Jang, and J. Han, *Phys. Rev. Lett.* **99**, 044501 (2007).
- [5] E. A. Demekhin, N. V. Nikitin, and V. S. Shelistov, *Phys. Fluids* **25**, 122001 (2013).
- [6] M. Wang and Q. Kang, *J. Comput. Phys.* **229**, 728 (2010).
- [7] I. Rubinstein and B. Zaltzman, *Phys. Rev. E* **62**, 2238 (2000).
- [8] I. Rubinstein and B. Zaltzman, *Math. Models Methods Appl. Sci.* **11**, 263 (2001).
- [9] I. Rubinstein and B. Zaltzman, *Phys. Rev. E* **68**, 032501 (2003).
- [10] I. Rubinstein, E. Staude, and O. Kedem, *Desalination* **69**, 101 (1988).
- [11] F. Maletzki, H. W. Rossler, and E. Staude, *J. Membr. Sci.* **71**, 105 (1992).
- [12] I. Rubinshtein, B. Zaltzman, J. Pretz, and C. Linder, *Russ. J. Electrochem.* **38**, 853 (2002).
- [13] G. Yossifon and H.-C. Chang, *Phys. Rev. Lett.* **101**, 254501 (2008).
- [14] B. Zaltzman and I. Rubinstein, *J. Fluid Mech.* **579**, 173 (2007).
- [15] E. A. Demekhin, E. M. Shapar, and V. V. Lapchenko, *Dokl. Phys.* **53**, 450 (2008).
- [16] E. A. Demekhin, S. V. Polyanskikh, and Y. M. Shtemler, [arXiv:1001.4502](https://arxiv.org/abs/1001.4502).
- [17] E. N. Kalaidin, S. V. Polyanskikh, and E. A. Demekhin, *Dokl. Phys.* **55**, 502 (2010).
- [18] H. Lin, *Mech. Res. Commun.* **36**, 33 (2009).
- [19] A. Ajdari, *Phys. Rev. Lett.* **75**, 755 (1995).
- [20] A. Karimi and M. R. Paul, *Phys. Rev. E* **85**, 046201 (2012).
- [21] E. A. Demekhin, V. S. Shelistov, and S. V. Polyanskikh, *Phys. Rev. E* **84**, 036318 (2011).
- [22] V. S. Shelistov, N. V. Nikitin, G. S. Ganchenko, and E. A. Demekhin, *Dokl. Phys.* **56**, 538 (2011).
- [23] H.-C. Chang, E. A. Demekhin, and V. S. Shelistov, *Phys. Rev. E* **86**, 046319 (2012).
- [24] V. S. Pham, Z. Li, K. M. Lim, J. K. White, and J. Han, *Phys. Rev. E* **86**, 046310 (2012).
- [25] C. L. Druzgalski, M. B. Andersen, and A. Mani, *Phys. Fluids* **25**, 110804 (2013).
- [26] S. M. Davidson, M. B. Andersen, and A. Mani, *Phys. Rev. Lett.* **112**, 128302 (2014).
- [27] H.-C. Chang, E. A. Demekhin, and S. S. Saprikin, *J. Fluid Mech.* **462**, 255 (2002).
- [28] N. V. Nikitin, *Int. J. Numer. Methods Fluids* **51**, 221 (2006).
- [29] I. Rubinstein and L. Shtilman, *J. Chem. Soc. Faraday Trans. 2* **75**, 231 (1979).
- [30] M. C. Cross and P. G. Hohenberg, *Rev. Mod. Phys.* **65**, 851 (1993).
- [31] *Cellular Structures in Instabilities*, proceedings, edited by J. E. Wesfreid and S. Zaleski (Springer, Berlin, 1984).
- [32] A. A. Nepomnyashchy, M. G. Velarde, and P. Colinet, *Interfacial Phenomena and Convection* (Chapman & Hall/CRC, London, 2002).
- [33] <http://demekhin.kubannet.ru/electrokinetic.php>
- [34] P. D. Wedman, H. Linde, and M. G. Velarde, *Phys. Fluids A* **4**, 921 (1992).
- [35] H. Linde, X. Chu, and M. G. Velarde, *Phys. Fluids A* **5**, 1068 (1993).
- [36] H.-C. Chang, E. A. Demekhin, and E. N. Kalaidin, *J. Fluid Mech.* **294**, 123 (1995).